Corresponding author: Laura Di Gesu
laura.digesu@est.asi.it

Corresponding author: Immacolata Donnarumma
immacolata.donnarumma@asi.it

Corresponding author: Fabrizio Tavecchio
fabrizio.tavecchio@inaf.it

The X-ray Polarization View of Mrk 421 in an Average Flux State as Observed by the *Imaging X-ray Polarimetry Explorer*

Laura Di Gesu,[1] Immacolata Donnarumma,[2] Fabrizio Tavecchio,[3] Iván Agudo,[4] Thibault Barnounin,[5] Nicolò Cibrario,[6,7] Niccolò Di Lalla,[8] Alessandro Di Marco,[9] Juan Escudero,[4] Manel Errando,[10] Svetlana G. Jorstad,[11,12] Dawoon E. Kim,[9,13,14] Pouya M. Kouch,[15,16] Ioannis Liodakis,[15] Elina Lindfors,[15] Grzegorz Madejski,[8] Herman L. Marshall,[17] Alan P. Marscher,[11] Riccardo Middei,[18,19] Fabio Muleri,[9] Ioannis Myserlis,[20] Michela Negro,[21,22,23] Nicola Omodei,[8] Luigi Pacciani,[9] Alessandro Paggi,[6] Matteo Perri,[18,19] Simonetta Puccetti,[18] Lucio A. Antonelli,[19,18] Matteo Bachetti,[24] Luca Baldini,[25,26] Wayne H. Baumgartner,[27] Ronaldo Bellazzini,[25] Stefano Bianchi,[28] Stephen D. Bongiorno,[27] Raffaella Bonino,[7,6] Alessandro Brez,[25] Niccolò Bucciantini,[29,30,31] Fiamma Capitanio,[9] Simone Castellano,[25] Elisabetta Cavazzuti,[2] Stefano Ciprini,[32,18] Enrico Costa,[9] Alessandra De Rosa,[9] Ettore Del Monte,[9] Victor Doroshenko,[33,34] Michal Dovčiak,[35] Steven R. Ehlert,[27] Teruaki Enoto,[36] Yuri Evangelista,[9] Sergio Fabiani,[9] Riccardo Ferrazzoli,[9] Javier A. Garcia,[37] Shuichi Gunji,[38] Kiyoshi Hayashida,[39] Jeremy Heyl,[40] Wataru Iwakiri,[41] Vladimir Karas,[35] Takao Kitaguchi,[36] Jeffery J. Kolodziejczak,[27] Henric Krawczynski,[42] Fabio La Monaca,[9] Luca Latronico,[7] Simone Maldera,[7] Alberto Manfreda,[25] Frédéric Marin,[5] Andrea Marinucci,[1] Francesco Massaro,[7,6] Giorgio Matt,[28] Ikuyuki Mitsuishi,[43] Tsunefumi Mizuno,[44] C.-Y. Ng,[45] Stephen L. O'Dell,[27] Chiara Oppedisano,[7] Alessandro Papitto,[19] George G. Pavlov,[46] Abel L. Peirson,[8] Melissa Pesce-Rollins,[25] Pierre-Olivier Petrucci,[47] Maura Pilia,[24] Andrea Possenti,[24] Juri Poutanen,[16,34] Brian D. Ramsey,[27] John Rankin,[9] Ajay Ratheesh,[9] Roger W. Romani,[8] Carmelo Sgrò,[25] Patrick Slane,[48] Paolo Soffitta,[9] Gloria Spandre,[25] Toru Tamagawa,[36] Roberto Taverna,[49] Yuzuru Tawara,[43] Allyn F. Tennant,[27] Nicolas E. Thomas,[27] Francesco Tombesi,[14,32,50] Alessio Trois,[24] Sergey Tsygankov,[16,34] Roberto Turolla,[49,51] Jacco Vink,[52] Martin C. Weisskopf,[27] Kinwah Wu,[51] Fei Xie,[9,53] and Silvia Zane[51]

[1]ASI -Agenzia Spaziale Italiana, Via del Politecnico snc, 00133 Roma, Italy
[2]ASI - Agenzia Spaziale Italiana, Via del Politecnico snc, 00133 Roma, Italy
[3]INAF Osservatorio Astronomico di Brera, Via E. Bianchi 46, 23807 Merate (LC), Italy
[4]Instituto de Astrofísica de Andalucía-CSIC, Glorieta de la Astronomía s/n, 18008, Granada, Spain
[5]Université de Strasbourg, CNRS, Observatoire Astronomique de Strasbourg, UMR 7550, 67000 Strasbourg, France
[6]Dipartimento di Fisica, Università degli Studi di Torino, Via Pietro Giuria 1, 10125 Torino, Italy
[7]Istituto Nazionale di Fisica Nucleare, Sezione di Torino, Via Pietro Giuria 1, 10125 Torino, Italy
[8]Department of Physics and Kavli Institute for Particle Astrophysics and Cosmology, Stanford University, Stanford, California 94305, USA
[9]INAF Istituto di Astrofisica e Planetologia Spaziali, Via del Fosso del Cavaliere 100, 00133 Roma, Italy
[10]Physics Department and McDonnell Center for the Space Sciences, Washington University in St. Louis, St. Louis, MO63130, USA
[11]Institute for Astrophysical Research, Boston University, 725 Commonwealth Avenue, Boston, MA 02215, USA
[12]Department of Astrophysics, St. Petersburg State University, Universitetsky pr. 28, Petrodvoretz, 198504 St. Petersburg, Russia
[13]Dipartimento di Fisica, Università degli Studi di Roma "La Sapienza", Piazzale Aldo Moro 5, 00185 Roma, Italy
[14]Dipartimento di Fisica, Università degli Studi di Roma "Tor Vergata", Via della Ricerca Scientifica 1, 00133 Roma, Italy
[15]Finnish Centre for Astronomy with ESO, 20014 University of Turku, Finland
[16]Department of Physics and Astronomy, 20014 University of Turku, Finland
[17]MIT Kavli Institute for Astrophysics and Space Research, Massachusetts Institute of Technology, 77 Massachusetts Avenue, Cambridge, MA 02139, USA
[18]Space Science Data Center, Agenzia Spaziale Italiana, Via del Politecnico snc, 00133 Roma, Italy
[19]INAF Osservatorio Astronomico di Roma, Via Frascati 33, 00078 Monte Porzio Catone (RM), Italy
[20]Institut de Radioastronomie Millimétrique, Avenida Divina Pastora, 7, Local 20, E–18012 Granada, Spain
[21]University of Maryland, Baltimore County, Baltimore, MD 21250, USA
[22]NASA Goddard Space Flight Center, Greenbelt, MD 20771, USA
[23]Center for Research and Exploration in Space Science and Technology, NASA/GSFC, Greenbelt, MD 20771, USA
[24]INAF Osservatorio Astronomico di Cagliari, Via della Scienza 5, 09047 Selargius (CA), Italy
[25]Istituto Nazionale di Fisica Nucleare, Sezione di Pisa, Largo B. Pontecorvo 3, 56127 Pisa, Italy
[26]Dipartimento di Fisica, Università di Pisa, Largo B. Pontecorvo 3, 56127 Pisa, Italy
[27]NASA Marshall Space Flight Center, Huntsville, AL 35812, USA
[28]Dipartimento di Matematica e Fisica, Università degli Studi Roma Tre, Via della Vasca Navale 84, 00146 Roma, Italy
[29]INAF Osservatorio Astrofisico di Arcetri, Largo Enrico Fermi 5, 50125 Firenze, Italy

[30] *Dipartimento di Fisica e Astronomia, Università degli Studi di Firenze, Via Sansone 1, 50019 Sesto Fiorentino (FI), Italy*

[31] *Istituto Nazionale di Fisica Nucleare, Sezione di Firenze, Via Sansone 1, 50019 Sesto Fiorentino (FI), Italy*

[32] *Istituto Nazionale di Fisica Nucleare, Sezione di Roma "Tor Vergata", Via della Ricerca Scientifica 1, 00133 Roma, Italy*

[33] *Institut fü r Astronomie und Astrophysik, Universität Tübingen, Sand 1, 72076 Tübingen, Germany*

[34] *Space Research Institute of the Russian Academy of Sciences, Profsoyuznaya Str. 84/32, Moscow 117997, Russia*

[35] *Astronomical Institute of the Czech Academy of Sciences, Boční II 1401/1, 14100 Praha 4, Czech Republic*

[36] *RIKEN Cluster for Pioneering Research, 2-1 Hirosawa, Wako, Saitama 351-0198, Japan*

[37] *California Institute of Technology, Pasadena, CA 91125, USA*

[38] *Yamagata University,1-4-12 Kojirakawa-machi, Yamagata-shi 990-8560, Japan*

[39] *Osaka University, 1-1 Yamadaoka, Suita, Osaka 565-0871, Japan*

[40] *University of British Columbia, Vancouver, BC V6T 1Z4, Canada*

[41] *Department of Physics, Faculty of Science and Engineering, Chuo University, 1-13-27 Kasuga, Bunkyo-ku, Tokyo 112-8551, Japan*

[42] *Physics Department and McDonnell Center for the Space Sciences, Washington University in St. Louis, St. Louis, MO 63130, USA*

[43] *Graduate School of Science, Division of Particle and Astrophysical Science, Nagoya University, Furo-cho, Chikusa-ku, Nagoya, Aichi 464-8602, Japan*

[44] *Hiroshima Astrophysical Science Center, Hiroshima University, 1-3-1 Kagamiyama, Higashi-Hiroshima, Hiroshima 739-8526, Japan*

[45] *Department of Physics, The University of Hong Kong, Pokfulam, Hong Kong*

[46] *Department of Astronomy and Astrophysics, Pennsylvania State University, University Park, PA 16802, USA*

[47] *Université Grenoble Alpes, CNRS, IPAG, 38000 Grenoble, France*

[48] *Center for Astrophysics, Harvard & Smithsonian, 60 Garden St, Cambridge, MA 02138, USA*

[49] *Dipartimento di Fisica e Astronomia, Università degli Studi di Padova, Via Marzolo 8, 35131 Padova, Italy*

[50] *Department of Astronomy, University of Maryland, College Park, Maryland 20742, USA*

[51] *Mullard Space Science Laboratory, University College London, Holmbury St Mary, Dorking, Surrey RH5 6NT, UK*

[52] *Anton Pannekoek Institute for Astronomy & GRAPPA, University of Amsterdam, Science Park 904, 1098 XH Amsterdam, The Netherlands*

[53] *Guangxi Key Laboratory for Relativistic Astrophysics, School of Physical Science and Technology, Guangxi University, Nanning 530004, China*

Abstract

Particle acceleration mechanisms in supermassive black hole jets, such as shock acceleration, magnetic reconnection, and turbulence, are expected to have observable signatures in the multi-wavelength polarization properties of blazars. The recent launch of the *Imaging X-ray Polarimetry Explorer* (*IXPE*) enables us, for the first time, to use polarization in the X-ray band (2-8 keV) to probe the properties of the jet synchrotron emission in high-frequency-peaked BL Lac objects (HSPs). We report the discovery of X-ray linear polarization (degree $\Pi_x = 15\pm2\%$ and electric-vector position angle $\psi_x = 35\pm4°$) from the jet of the HSP Mrk 421 in an average X-ray flux state. At the same time, the degree of polarization at optical, infrared, and millimeter wavelengths was found to be lower by at least a factor of 3. During the *IXPE* pointing, the X-ray flux of the source increased by a factor of 2.2, while the polarization behavior was consistent with no variability. The higher level of Π_x compared to longer wavelengths, and the absence of significant polarization variability, suggest a shock as the most likely X-ray emission site in the jet of Mrk 421 during the observation. The multiwavelength polarization properties are consistent with an energy-stratified electron population, where the particles emitting at longer wavelengths are located farther from the acceleration site, where they experience a more disordered magnetic field.

1. INTRODUCTION

Relativistic extragalactic jets expelled by active galactic nuclei (AGNs) are the most powerful persistent emitters in the Universe (e.g., Blandford et al. 2019). The understanding of their physical structure, dynamics, and impact on the surrounding environment plays a fundamental role in our view of black holes, galaxies, and clusters. The current framework (e.g., Tchekhovskoy et al. 2011; Komissarov et al. 2007) assumes that jets are accelerated and collimated by magnetic stresses act-

ing close to the central black hole. As the jet propagates, magnetic flux is progressively converted into kinetic flux, accelerating the flow. The dissipation of a fraction of the (magnetic and/or kinetic) energy flux provides the energy required to accelerate particles to ultrarelativistic energies. These particles produce extremely luminous emission across the electromagnetic spectrum.

Jets are most prominent when the outflow velocity is nearly aligned with the line-of-sight and the emission is consequently boosted by relativistic effects. This occurs in blazars, AGNs characterized by powerful, variable (with time-scales as short as a few minutes in the most extreme cases), non-thermal emission extending from radio waves to γ rays (e.g. Romero et al. 2017). The spectral energy distribution (SED) of blazars displays two broad components that are ascribed to synchrotron radiation peaking at IR to X-ray frequencies and Compton scattering with maximum at γ-ray energies (but see, e.g., Böttcher et al. 2013 for an alternative hadronic interpretation), respectively. Blazars in which the synchrotron luminosity peaks at X-ray energies are termed high-synchrotron-peaked BL Lacertae objects (HSPs or HBLs), the prototype of which is Mrk 421.

The precise nature of the processes responsible for the acceleration of high-energy particles remains unclear (see Matthews et al. 2020 for a review). Shocks are likely to occur in blazar jets, where particles can be accelerated through the well-studied diffusive shock acceleration (DSA) process (e.g., Blandford & Eichler 1987). However, shocks are unlikely to be efficient if the jet is highly magnetized (Sironi et al. 2015). In that case, it is more likely that particles are accelerated through conversion of magnetic energy in reconnection events (e.g. Sironi & Spitkovsky 2014). Polarimetric analysis of the synchrotron emission, which provides information on the geometry and structure of magnetic fields, can help to specify which acceleration process dominates (e.g., Tavecchio 2021, and references therein). Measurement of linear polarization at X-ray energies from HSPs is particularly important, since it probes the highest-energy electrons, which radiate close to the acceleration site. Simultaneous observations of polarization at optical and longer wavelengths then allow comparisons of the physical conditions experienced by these electrons with those of regions where only lower-energy particles are present. The results can then be used to test the proposed models for particle acceleration in blazar jets. Previous polarization measurements of blazars have been limited to frequencies below those where the synchrotron emission of an HSP peaks. The Imaging X-ray Polarimetry Explorer (Weisskopf 2022), a joint NASA and Italian Space Agency (ASI) mission launched on

2021 December 9, is the first telescope capable of measuring the polarization of blazars at X-ray energies. The *IXPE* payload comprises three X-ray telescopes with three Gas Pixel Detector Units (DUs, Costa et al. 2001; Soffitta et al. 2021) in the focal planes, sensitive to linear polarization in the 2-8 keV energy band. Liodakis et al. (2022, submitted) have reported detection of X-ray polarization by *IXPE* in the HSP Mrk 501. Here we report the first *IXPE* observation of Mrk 421 (redshift $z = 0.0308$). This source is a relatively nearby HSP that has been intensively studied at many wavelengths (e.g., Abdo et al. 2011; MAGIC Collaboration et al. 2021). The source possesses significant variability in the optical parameters of polarization. For instance, Marscher & Jorstad (2021) reported that during intensive optical polarization sampling in April-May 2017, Mrk 421 exhibited variations in polarization degree Π_o between 6 and 11% and changes in electric vector position angle Ψ_o by $\sim 50°$ on a timescale of 1-2 days. Mrk 421 is among the first blazars detected at both GeV (by EGRET onboard the *Compton* Gamma Ray Observatory; Lin et al. 1992) and TeV energies (by the Whipple Observatory; Punch et al. 1992). It is well-monitored in the X-ray band, where the synchrotron SED peaks at a high flux level, making it a prime target for linear polarization observations by *IXPE*.

2. X-RAY POLARIZATION ANALYSIS

2.1. *Time-averaged polarization properties*

IXPE observed Mrk 421 from 10:00 UTC on 2022 May 4 to 11:10 UTC on May 6, with a live-time exposure of 97 ks, alongside a multi-wavelength campaign. The latter included observations with the *Swift X-Ray Telescope* (XRT), *XMM-Newton* (*XMM*), and the *Nuclear Spectroscopic Telescope Array* (*NuSTAR*) at X-ray energies, the Nordic Optical Telescope at the optical R band, Boston University's Perkins Telescope at infrared (IR) wavelengths, and the Institut de Radioastronomie Millimétrique (*IRAM*) 30 m telescope at short millimeter wavelengths. The optical, IR, and radio flux densities and linear polarization measurements are summarized in Table 1. The data reduction procedure for all of the telescopes is described in Appendix A. At the epoch of the *IXPE* observation, the 0.3-10 keV X-ray flux of Mrk 421 was $\sim 3.5 \times 10^{-10}$ erg s^{-1} cm^{-2}, which is near its typical flux state (Liodakis et al. 2019). As a comparison, during occasional flaring events reaching gamma-ray energies, the X-ray flux of Mrk 421 can be ten times higher (Donnarumma et al. 2009).

We have determined the 2-8 keV polarization of Mrk 421 using (1) the Kislat et al. (2015) method within the ixpeobssim simulation and analysis software (Bal-

Table 1. Log of the observations of Mrk 421 used in this work.

Telescope	Band	Dates	Radio/Optical flux density	Radio/Optical Polarization	
	(eV)	(YYYY-MM-DD)	(erg s^{-1} cm^{-2} Hz^{-1})	$\Pi(\%)$	ψ (°)
Nordic Optical Telescope	R: 1.9	2022-05-04	$(1.9 \pm 0.03) \times 10^{-25}$	2.9 ± 0.1	21 ± 1
IRAM	3.5×10^{-4}	2022-05-05	$(2.8 \pm 0.1) \times 10^{-24}$	3.0 ± 0.7	57 ± 7
Perkins	H: 0.8	2022-05-05	$(3.94 \pm 0.03) \times 10^{-25}$	0.9 ± 0.3	39 ± 10
Perkins	H: 0.8	2022-05-06	$(4.48 \pm 0.03) \times 10^{-25}$	2.1 ± 0.6	39 ± 10
Perkins	H: 0.8	2022-05-07	$(4.20 \pm 0.04) \times 10^{-25}$	2.2 ± 0.5	32 ± 8
IRAM	3.5×10^{-4}	2022-05-07	$(3.8 \pm 0.2) \times 10^{-24}$	3.8 ± 0.7	52 ± 5
IRAM	9.5×10^{-4}	2022-05-07	$(2.5 \pm 0.1) \times 10^{-24}$	≤ 6	-
Telescope	Energy range	Dates	X-ray flux	X-ray Polarization	
	(keV)	(YYYY-MM-DD)	(erg s^{-1} cm^{-2})	$\Pi_x(\%)$	ψ_x (°)
Swift-XRT	0.3-10.0	2022-05-03	$(3.50 \pm 0.05) \times 10^{-10}$	-	-
XMM-Newton	0.5-10.0	2022-05-03	$(3.04 \pm 0.01) \times 10^{-10}$	-	-
IXPE	2.0-8.0	2022-05-04	$(8.67 \pm 0.03) \times 10^{-11}$	15 ± 2	35 ± 4
NuSTAR	3.0-30.0	2022-05-04	$(7.21 \pm 0.11) \times 10^{-10}$	-	-
Swift-XRT	0.3-10.0	2022-05-05	$(4.16 \pm 0.08) \times 10^{-10}$	-	-
Swift-XRT	0.3-10.0	2022-05-07	$(5.93 \pm 0.09) \times 10^{-10}$	-	-

dini et al. 2022), (2) a spectro-polarimetric fit of the *IXPE* data alone, (3) a spectro-polarimetric fit of combined quasi-simultaneous data from *IXPE*, the *XMM* EPIC-pn camera, and *NuSTAR*, (4) a maximum likelihood spectro-polarimetric (MLS) fit of the IXPE data, implemented within the multinest algorithm, and, (5) a maximum-likelihood calculation of the polarization properties based on the method of Marshall (2021). While the Kislat et al. (2015) approach and the maximum likelihood calculation are model independent, spectropolarimetric and MLS fits include modeling of the energy spectrum, allowing us to test whether the determination of the polarization properties is affected by the modeling of the spectral curvature. For Mrk 421, we find a minimum detectable polarization at 99% significance (MDP99) of 6.4% in the 2-8 keV band. The measured polarization parameters from the three combined detector units are $\Pi_x = 15 \pm 2$ % and $\psi_x = +35 \pm 4°$. Given the MDP99 level of the observation, the 2-8 keV polarization of Mrk 421 is detected at a confidence level of >99.99% (i.e., at a significance of 7σ). By computing the polarization properties in three energy bins, i.e., 2.0-3.0 keV, 3.0-4.0 keV, and 4.0-8.0 keV, we did not observe any significant variation of the polarization properties with photon energy within maximum error bars of $\pm 5\%$ and $\pm 8°$ for the polarization degree and polarization angle, respectively.

We have also determined the degree Π_x and position angle ψ_x of polarization via a spectro-polarimetric fit in Xspec (Arnaud et al. 1999) which implements the approach of Strohmayer (2017). In all of the fits, we included Galactic photo-electric absorption along the line
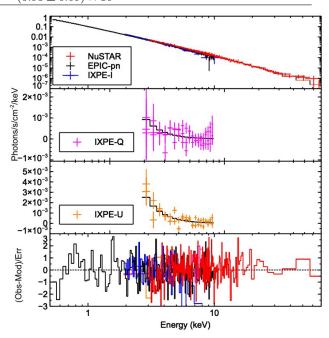

Figure 1. Spectro-polarimetric fit of the *NuSTAR* (red), *XMM* EPIC-pn (black), and *IXPE* (blue, magenta, and orange) spectra. From the top to the bottom, we show the fit of the I, Q, U spectra and the residuals of the best fit model (solid line). The spectral channels have been rebinned for clarity.

of sight toward Mrk 421 ($N_{\rm H}$ =1.34×10^{20} cm^{-2}; HI4PI Collaboration et al. 2016) using the TBABS model, with Fe abundances set according to Wilms et al. (2000). As a first test, we considered only the *IXPE* data (i.e., 3 Stokes parameters for 3 DUs). In the fit we consid-

ered multiplicative constants, free to vary, to account for inter-calibration differences among the three DUs. The shape of the I spectra is best fit ($\frac{\chi^2}{\text{d.o.f}}$=293/267) by a power law with photon index $\Gamma = 2.97 \pm 0.01$. By multiplying the model for the I spectra by a constant polarization model (polconst model in Xspec), we obtained a statistically acceptable spectropolarimetric fit of the I, Q, and U spectra ($\frac{\chi^2}{\text{d.o.f}}$=841/795). The fluxes measured by the three IXPE DUs agree with each other within 12%, with the differences explained by uncertainties in the $IXPE$ effective area at the time of observation. The estimated polarization degree and position angle, $\Pi_{\text{x}} = 16 \pm 2\%$ and $\psi_{\text{x}} = 34 \pm 3°$, are consistent with the ixpeobssim result.

Next, we used the simultaneous XMM-$Newton$ and $NuSTAR$ data to refine the constraints on the broadband spectral shape and check whether the derived polarization is sensitive to the addition of broad-band spectral curvature in the model of the energy spectrum. We initially fit the data from XMM EPIC-pn, $NuSTAR$ FPMA, and $NuSTAR$ FPMB plus the three $IXPE$ Stokes I spectra with a power-law model subject to photo-electric absorption (see above). We fixed the normalization and photon index Γ for all of the instruments, while we allowed five multiplicative constants to vary to account for cross-calibration between the instruments and source variability between the observations (see Table 1). This model does not provide a statistically acceptable fit to the broadband data ($\frac{\chi^2}{\text{d.o.f}}$=2764/611), which indicates that, when considering an energy range broader than that of $IXPE$, a more complex model of the spectral curvature is needed. The broad-band spectrum of Mrk 421 is better fit by a log-parabolic model (Massaro et al. 2004), in which the photon index varies as a log-parabola in energy i.e.

$$N(E) = K(E/E_{\text{p}})^{(\alpha - \beta \log (E/E_p))},$$

where the pivot energy E_{p} is a scaling factor, α describes the spectral slope at the pivot energy, β describes the spectral curvature and K is a normalization constant. This spectral shape is typical for HSP blazars, including Mrk 421, both in quiescence and in flaring states (e.g., Baloković et al. 2016; Donnarumma et al. 2009). As the photon index varies with the energy in this model, the choice of the reference energy E_{p} changes the determination of α. In our fits, we set the pivot energy E_{p} to 5.0 keV (e.g., Baloković et al. 2016), while the α and β parameters were allowed to vary, although they were coupled across the three telescopes. With our setup, α approximates the photon index in the 3.0-7.0 keV range (i.e., the core of the IXPE band).

Next, to determine the polarization properties from the polconst model, we added to the fit the IXPE Stokes Q and U spectra. This fitting exercise returned an estimation of the polarization parameters of $\Pi_{\text{x}} = 16 \pm 2\%$ and $\psi_{\text{x}} = 35 \pm 3°$, which is consistent with the ixpeobssim result and with the fit using only $IXPE$ data. As a final check, we tested whether allowing the spectral shape to differ between $NuSTAR$, XMM Epic-pn, and $IXPE$ could further improve the fit and thereby affect the values of Π_{x} and ψ_{x}. Decoupling the α and β parameters among the three instruments resulted in a statistically significant improvement of the fit ($\Delta\chi^2 = -72$ for 4 more d.o.f., corresponding to a decrease in the Bayesian information criterion ΔBIC=-43). This discrepancy in spectral shape between the three telescopes is likely due to non-simultaneity of the observations as the source varies (see §§2.2). We note however, that this fitting exercise returned the same result, within the uncertainty, for the polarization properties: $\Pi_{\text{x}} = 16 \pm 2\%$, $\psi_{\text{x}} = 34 \pm 4°$. This indicates that the polarization determination is robust against differences in the details of the spectral shape modeling. Our final spectropolarimetric fit, including XMM EPIC-pn, $NuSTAR$, and $IXPE$, is displayed in Fig. 1. To highlight the significance of the polarization detection and the agreement among the determinations via different methods that use different models for the spectral curvature in Fig. 2, we compared the two-dimensional confidence contours for the X-ray polarization obtained with ixpeobssim and with our spectropolarimetric fits.

Finally, for the MLS method, we fit the $IXPE$ data with a power-law model with Galactic photo-electric absorption (see above), while holding the intrinsic values of Q and U constant. In this way, we derived a photon index $\Gamma = 2.97 \pm 0.01$ and polarization properties ($\Pi_{\text{x}} = 16 \pm 2\%$ and $\psi_{\text{x}} = 34 \pm 2°$) consistent with the values from the previously described methods. In addition, using a model-independent maximum-likelihood calculation, we obtained $\Pi_{\text{x}} = 16 \pm 2\%$ and $\psi_{\text{x}} = 34 \pm 2°$. This is a further, independent confirmation of our polarization measurement of Mrk 421.

2.2. Polarization variability

To obtain additional information about the physical conditions in the jet of Mrk 421, we have searched for variability of the X-ray polarization properties as a function of time within the total duration of the $IXPE$ pointing. We first exploited the $Swift$ XRT monitoring of the source (9 separate pointings, each for ~ 1 ks) to sample the spectral evolution of the source before, during, and after the $IXPE$ pointing. As a comparison, we created a light curve of the $IXPE$ count rate with time bins of
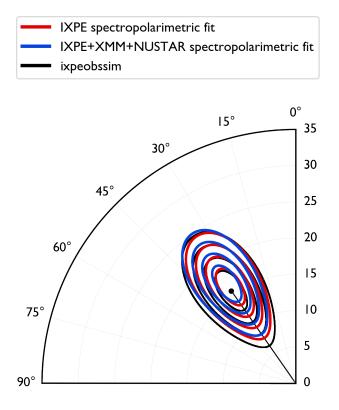
Figure 2. Polar plot of the Π_x-ψ_x plane. We show the confidence contours of X-ray polarization derived with ixpeobssim (black), a spectro-polarimetric fit of the IXPE data (red) and a spectro-polarimetric fit of the *IXPE*, *XMM* EPIC-pn, and *NuSTAR* data (blue). For each case, the contours at 68.3%, 95.4%, 99.7%, and 99.994% confidence level are shown.

10 ks (Fig. 3). The flux of the source increased during the *IXPE* pointing in both the soft (0.3-2 keV) and hard (2-10 keV) XRT bands, while maintaining the same spectral slope, as witnessed by the hardness ratio light curve. In the *IXPE* data, we find an increase of the count rate by a factor of 2.2.

To investigate whether there was also a variation in the polarization properties on different time-scales within the *IXPE* pointing, we proceeded as follows. Using time bins in the range 5-50 ks, we created light curves of the normalized Stokes parameters. For each case, we fit the light curve with a constant model and recorded the probability of the null hypothesis of obtaining a value of χ^2 at least as large as that of the constant model. For all of the time bins tested, we found that this probability is always above 1%, which indicates that the Stokes parameters are consistent with no variation during the *IXPE* pointing. We therefore conclude that, despite the increase in flux during the observation, the polarization properties did not vary substantially. As a useful quantitative constraint, we computed the uncertainty in Π_x and ψ_x allowed by the statistic in each
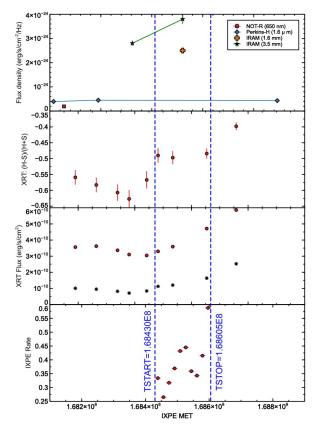

Figure 3. From the top to the bottom: light-curves of the optical, infrared and millimeter flux densities, light-curve of *Swift* XRT hardness ratio, light-curve of the soft (S band: 0.3-2.0 keV) and hard (H band: 2.0-10.0 keV) *Swift* XRT fluxes, and light-curve of the *IXPE* count rates. In the first panel, the legend displays the symbols for the different instruments and wavelengths. Multiple data points from the same instrument are connected by a line to guide the eye. In the third panel, soft and hard fluxes are coded as red circles and blue asteriks. The dashed vertical lines indicate the beginning and the end of the *IXPE* observation.

time bin. This is an indication of the amount of variation that can be excluded, on different time-scales, by the present analysis. On a time-scale of 50 ks, similar to 1-day time-scales sometimes used in studies of optical polarization variability (e.g., Blinov et al. 2015), variations in Π_x above $\sim \pm 4\%$ for a constant value of ψ_x, or variations in ψ_x above $\sim \pm 7°$ for constant Π_x, are excluded by the present analysis.

3. DISCUSSION

In optically-thin synchrotron sources, such as Mrk 421 at IR to X-ray wavelengths, the degree of polarization Π is a measure of the level of disorder of the magnetic field, while ψ is perpendicular to the mean magnetic field direction as projected onto the sky plane. The dependence of the polarization on wavelength relates to the mecha-
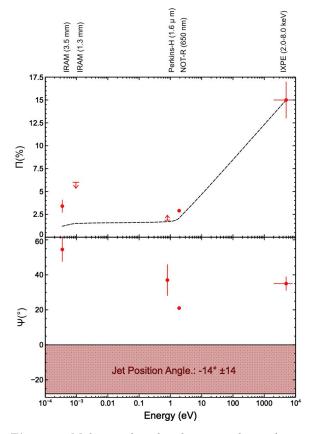
Figure 4. Multi-wavelength polarization degree (top panel) and angle (low panel) of Mrk 421 as a function of energy. The red circles represent detections, while the arrows indicate upper or lower limits. The instruments that provided each measurement are labeled on top. The dashed line represents theoretical estimations assuming the formalism of Hughes & Miller (1991) for a turbulent jet. In the second panel, the horizontal shaded area indicates the time-averaged jet position angle and its uncertainty, measured with the Very Long Baseline Array at 43 GHz (Weaver et al. 2022).

nism that accelerates the particles in situ. In a highly magnetized jet, conversion of magnetic into kinetic energy is a viable mechanism to accelerate the particles. If the emission is modulated by the development of a large-scale kink instability, relatively high (e.g., ∼20%) X-ray and optical polarization is predicted, with both Π and ψ smoothly modulated with time (e.g., Bodo et al. 2021). On the other hand, when single current sheets are responsible for most of the observed emission, large and rapid variability is expected, leading to substantial dilution of the polarization when integrated over long exposures. In this case, one expects to measure a lower degree of polarization in the X-rays than in the optical band (Zhang et al. 2021).

In contrast, in the case of weakly magnetized jets, a shock is a more likely acceleration mechanism. According to several models (Marscher & Gear 1985; Tavecchio

et al. 2018; Angelakis et al. 2016), if particles are accelerated at a shock front and advected downstream, the emission at the shortest (X-ray) wavelength is produced by energetic particles that are present only very close to the shock front. Longer-wavelength emission extends over a larger volume that contains the lower-energy particles. If the magnetic field direction changes, or level of disorder increases, over the larger volume downstream of the acceleration site, Π_x at shorter wavelengths is expected to be higher than the degree of polarization at longer wavelengths. If the plasma in the jet flow is highly turbulent before crossing the shock, the field will be partially ordered parallel to the shock front, while the flux, Π, and ψ should be time-variable (although the average value of ψ should remain parallel to the jet axis), more strongly so at X-ray than at longer wavelengths (Marscher 2014). Under these conditions, the erratic variability of both degree and angle of polarization can potentially lead the X-ray polarization vectors to average to low values in day-long observations (Di Gesu et al. 2022). If the flow only becomes turbulent after crossing the shock, the time variability can be weak, but Π should decrease toward longer wavelengths. If we assume that synchrotron losses dominate the radiative energy losses, the timescale of the losses is inversely proportional to the Doppler factor, δ, frequency, ν, and strength of the magnetic field, B, as $\tau_{\rm loss} \propto [(1+z)/(\delta\nu B^3)]^{1/2}$ (Marscher & Gear 1985). If δ and B are the same across the X-ray/optical/IR regions (and possibly less in the site of millimeter-wave emission), the size of the regions behind the shock with respect to the size of the X-ray emission region can be determined as $R_\nu = R_X(\nu_X/\nu)^{1/2}$. If we consider the magnetic field be turbulent, according to the formalism suggested by Hughes & Miller (1991), the IXPE measurement implies that the X-ray emission should consist of ∼30 cells with different magnetic field directions. Therefore, within this interpretation, we can estimate the sizes (in terms of number of cells) and polarization of the optical, IR, 1.3mm, and 3mm regions. We find predicted values of Π equal to 2.1%, 1.7%, 1.5%, and 1.2% in R band, H band and at 1.3mm and 3mm, respectively.

In Figure 4 we summarize the multi-wavelength polarization properties that we have measured for Mrk 421 during an average state in 2022 May. The degree of polarization in the X-ray band is higher by a factor of ∼5 than in the optical and by at least a factor ∼3 than at IR and millimeter wavelengths. This is in qualitative agreement with the energy-stratified shock model described above, although the theoretically predicted values of Π are somewhat lower than the measured values if we use the degree of X-ray polarization as a reference. In addi-

tion, shock acceleration is favored by the observed temporal stability of the polarization properties (§2.2). This is a natural prediction of, e.g., a shock model with a self-generated magnetic field (Tavecchio 2021), while it is in tension with magnetic reconnection models, which predict smooth (Bodo et al. 2021), or even rapid (Zhang et al. 2018), polarization variability, including polarization angle swings.

One can see in Figure 4 that there is a discrepancy between the multi-wavelength ψ values and the time-averaged[1] jet position angle measured at 43 GHz with the Very Long Baseline Array ($-14° \pm 14°$, Weaver et al. 2022). In contrast, although there are exceptions, the optical polarization position angle of BL Lac objects is frequently found to align (within $\pm 20°$) with that of the core of the jet (Marscher & Jorstad 2021). This has been ascribed to an ordered component of the magnetic field (e.g. a helical magnetic field compressed by a shock) aligned perpendicular to the jet axis. However, the jet of Mrk 421 has a wide opening angle of $\sim 60°$, owing mainly to projection effects caused by a small angle to the line of sight (Weaver et al. 2022). It is possible that the jet bends by tens of degrees on the smallest scales, such that there is a closer correspondence between Ψ and the jet direction where the X-ray and optical emission occurs. Future very long baseline interferometry at 1 mm wavelength can determine whether this is the case. Misalignments between the polarization angle and the jet direction, possibly induced by local disturbances of the magnetic field, have been reported for the variable radio knots of Mrk 421 (Piner & Edwards 2005).

4. CONCLUSIONS

The primary findings of the first *IXPE* observations of X-ray polarization from Mrk 421 in an average flux states are that (1) the degree of X-ray polarization was $15 \pm 2\%$, several times higher than at optical/infared/millimeter wavelengths; (2) the polarization properties were steady, while the X-ray flux rose by a factor of 2.2, during the $\sim$ 2-day *IXPE* pointing; and (3) the X-ray electric-vector position angle was $+35 \pm 4°$, close to the optical value of $+21 \pm 1°$, but different from the jet direction of $-14 \pm 14°$ measured at 43 GHz.

The finding of high X-ray polarization compared to longer wavelengths implies that the particles in the jet of Mrk 421 are energy-stratified. The higher-energy particles responsible for the emission at higher (X-ray) frequencies are located closer to the acceleration site, since their energy decays more rapidly than is the case for

lower-energy particles. As the particles stream away from the acceleration site, their energies decrease, so there is a negative gradient of maximum frequency of synchrotron radiation with distance from the acceleration region. If the particles encounter a more disordered magnetic field as they advect downstream, the degree of polarization then decreases toward longer wavelengths. The lack of polarization variation as the X-ray flux increases suggests that particles are injected in a region with stable magnetic field properties. Partially ordered magnetic fields can be produced close to the shock because of plasma processes (Tavecchio et al. 2018) or compression (Hughes et al. 1985). In this case, ψ should align with the jet axis, as found in Mrk 501 (Liodakis et al. 2022, submitted). The increase in the level of disorder of the field with distance from the shock can be caused by turbulence. However, our finding of little or no variation of the X-ray polarization properties on a timescale of 2 days, in contrast with the finding of monitoring of the optical polarization variability (Marscher & Jorstad 2021), suggests that the IXPE observation occurred during a time when the turbulence happened to be strong but stable.

Given the above expectations of theoretical models, our findings imply that shock acceleration is the most likely particle acceleration mechanism in the jet of Mrk 421 during the observation reported here. The "harder-when-brighter" spectral behavior that is commonly displayed by HSPs in the X-ray band, and that we also observed in our Swift monitoring of Mrk 421 (Fig. 3), is widely interpreted as due to the injection of fresh high-energy electrons by a shock (Kirk et al. 1998).

The discrepancy that we have found between the radio jet position angle and the millimeter/optical/infrared/X-ray polarization angle suggests that either the radio emission region is detached from the X-ray emission region, as is common in one-zone models where the X-ray emitting region is opaque at radio frequencies (e.g., Ghisellini & Tavecchio 2009), or that the jet bends between the sites of high- and low-frequency emission (Marscher 2008). Using the formalism of Hughes & Miller (1991) for a turbulent jet, we have estimated the optical/infrared/millimeter Π values that are implied by the X-ray measurement. These are somewhat lower than the observed values (Fig. 4), which suggests that the magnetic field behind the shock is not completely turbulent, but instead includes an ordered component.

Our study is part of a fundamental early attempt to explore the polarization properties of blazars over a wide range of wavelengths, now including X-rays. An important aspect of this is to determine whether, and in what

---

[1] See http://www.bu.edu/blazars/VLBA_GLAST/1101.html for the multi-epoch variability of the jet position angle.

manner, the polarization varies. However, the dearth of exactly simultaneous sampling at X-ray and optical wavelengths in the present study, and the limited sensitivity of the *IXPE* data to variations on short time-scales, prevent us from drawing firm general conclusions from this single realization. Multi-wavelength polarization monitoring of blazars on different time-scales is needed to probe more thoroughly the particle distribution and magnetic field dynamics in astrophysical jets, for example by searching for correlated variability patterns and time delays between the polarization light curves in different bands. In the future, the X-ray polarization information provided by *IXPE* will play a key role in these types of studies by adding to the existing probes valuable information on the location and physical conditions experienced by freshly accelerated high-energy particles.

Software: Xspec version 12.12.1   *Facilities:* *IXPE*, Nordic Optical Telescope, *NuS-TAR Swift*, *XMM-Newton*, Perkins Telescope Observatory

APPENDIX

A. IXPE AND MULTI-WAVELENGTH DATA ANALYSIS

A.1. *IXPE data*

IXPE data are processed using a pipeline[2] that estimates the photo-electron emission direction, correcting for charging effects, detector temperature, gas electron multiplier (GEM) gain non-uniformity, and polarization artifacts induced by spurious instrumental modulation (Rankin et al. 2022). The level-2 event files (one for each of the three DUs) produced by the pipeline contain all of the information typical of an imaging X-ray astronomy mission (e.g., photon arrival time, detector coordinates, and energy), with the addition of the polarization information in the form of event-by-event Stokes parameters. Before proceeding with the science analysis, we corrected the data for small time-dependent changes to the gain correction obtained from data taken with the on-board calibration sources (Ferrazzoli et al. 2020) close to the actual time of observation.

We performed the scientific analysis of the *IXPE* data using the ixpeobssim software (Pesce-Rollins et al. 2019; Baldini et al. 2022). At the angular resolution of *IXPE* ($\sim 30''$), blazars like Mrk 421 are point-like sources. The selection of *IXPE* events was performed with the xpselect tool, which applies to the photon lists a user-defined selection on sky position, time, phase, and energy. In the case of Mrk 421, we extracted the source events using circular regions $60''$in radius, while we used an annulus centered on the source, with an in inner and outer radius of $2'$and $5'$, respectively, to estimate the background. We found that the background accounts for less than 2% of the total counts in the source region, hence background subtraction is not critical for the polarization measurement. The Kislat et al. (2015) method for estimating the polarization of a user-defined set of events is implemented in the PCUBE algorithm. We created the Stokes-parameter spectra of the source using the PHA1, PHAU, and PHAQ alghoritms, which map the I, Q, and U Stokes parameters of the photons into OGIP-compliant PHA spectral files (3 Stokes-parameter spectra per 3 detector units). We prepared the spectra for the spectro-polarimetric fit by binning the I spectrum, requiring that a minimum of 30 counts is reached in each energy bin. This is needed for correctly using the χ^2statistics in the fit. Hence, as a last step, we applied the same binning to the Q and U spectra.

A.2. *Spectroscopic X-ray data*

In order to catch any possible X-ray flux variations of the source contemporaneous with the *IXPE* pointing, and to accurately constrain the slope of the X-ray spectrum, we observed Mrk 421 in the 0.3-10 keV energy band with the *Swift* XRT (9 pointings, each with exposure time ~ 1 ks, of which one was simultaneous with *IXPE*), and with *NuSTAR* in the 3-70 keV energy range (see Table 1). In addition, an *XMM-Newton* (5 ks) observation was carried out as a part of our program on 2022 May 3, one day before the *IXPE* pointing.
The *Swift* XRT observations were performed in Windowed Timing (WT) mode, and the data were processed with the X-Ray Telescope Data Analysis Software (XRTDAS, v. 3.6.1). In the analysis, we used the latest calibration files available in the *Swift* XRT CALDB (version 20210915). The X-ray source spectrum was extracted from the cleaned event file using a circular region with a radius of $47''$. The background was extracted using a circular region with the same radius from a blank-sky WT observation available in the *Swift* archive. As a final step, we binned the 0.3-10 keV channels to achieve at least 25 counts in each energy bin.
We calibrated and cleaned the *NuSTAR* data using the *NuSTAR* Data Analysis Software (NuSTARDAS, v. 2.1.1) and the latest calibration data files in the *NuSTAR* CALDB (version 20220301). The net exposure time after cleaning the dataset was 25 ks. For both the FPMA and FBMB detectors, we created level 2 cleaned event files with the nupipeline task, while high-level scientific data products were extracted using the nuproducts tool. We extracted the source spectrum from a circular region with a radius of $70''$, while we used an annular region to estimate the background.

---

[2] https://heasarc.gsfc.nasa.gov/docs/ixpe/analysis/
   IXPE-SOC-DOC-009-UserGuide-Software.pdf

Finally, we binned the spectra to achieve at least 50 counts in each energy bin.

The *XMM-Newton* observation of Mrk 421 was obtained in timing mode, which limits photon pile-up. We performed the data reduction using the XMM-Newton Science Analysis Software (SAS), version 20, and the latest calibration products. Starting from the raw observation data files (ODFs), we created the calibrated EPIC-pn event list using the SAS task epchain. To determine good time intervals (GTIs) free from background flares, we cut the time intervals where the light-curve of the background in the 10-13 keV band was above a fixed treshold of 0.4 counts/s (SAS task tabgtigen). In the clean event files, we selected the source and the background using boxed regions (with a width of 27 pixels) that maximize the signal-to-noise ratio. We created the source and background spectra using only single and double events, and we created the spectral response matrices using the SAS task rmfgen and arfgen. Finally, we prepared the spectrum for analysis by binning the energy channels to achieve at least 30 counts in each spectral bin. The model fitting to the spectrum was carried out with Xspec version 12.12.1, as described in the main text. To allow simultaneous spectro-polarimetric fitting with EPIC-pn and *NuSTAR*, we added to keyword "XFLT0001 Stokes:0" to the header of the non-*IXPE* pha files. This allowed Xspec to identify the spectra as I Stokes spectra.

A.3. *Optical and infrared data*

Optical polarization observations were performed using the Alhambra Faint Object Spectrograph and Camera (AL-FOSC) mounted at the 2.5 m Nordic Optical Telescope (NOT) on the night of 2022 May 4 (MJD 59703) in the R band (λ=6500 Å/E=1.9 eV, *FWHM*=1300 Å/0.4 eV). The data were obtained in the standard polarimetric mode and analyzed using a $2.5''$ aperture radius and standard photometric procedures included in the pipeline developed at Tuorla Observatory (Hovatta et al. 2016; Nilsson et al. 2018). Unpolarized and polarized standard stars were also used for calibration. The R magnitude of the source was 12.98 ± 0.02, which corresponds to $I = 19.8 \pm 0.3$ mJy, while $\Pi_{O,obs} = 2.42 \pm 0.06\%$ and $\psi_O = 21 \pm 1$. For the $2.5''$ aperture used in the analysis, the host galaxy contributes $I_{host} = 3.2 \pm 0.4$ mJy to the total emission (Nilsson et al. 2007). We correct for the host galaxy contamination of the polarization degree by subtracting the host-galaxy flux density as $\Pi_{intr} = \Pi_{obs} \times I/(I - I_{host})$ (Hovatta et al. 2016). The intrinsic polarization is therefore $\Pi_{O,int} = 2.9 \pm 0.1\%$.

Infrared observations in the H band were obtained at the Boston University 1.8 m Perkins telescope located in Flagstaff, AZ (Perkins Telescope Observatory, PTO, BU) using the IR camera MIMIR[3] on 2022 May 5, 6, and 9. Each observation consisted of 6 dithering exposures of 5 s each at 16 positions of a half-wave plate, rotated in steps of $22.5°$ from 0 to 360 °. The camera and data reduction procedures are described in detail by Clemens et al. (2012) The H-band degree of polarization changed from 1% to 2.2%, with average 1σ uncertainty of 0.5%. However, the Π measurements in H band are lower limits, since the level of contamination from the host galaxy is unknown. The position angle of polarization in H band agrees within the uncertainty with that of the IXPE observation.

A.4. *Millimeter-wave data*

Radio polarization at 3.5 mm (86.24 GHz) and 1.3 mm (230 GHz) was measured with the 30 m Telescope of the Institut de Radioastronomie Millimétrique (IRAM), located at the Pico Veleta Observatory (Sierra Nevada, Granada, Spain), on 2022 May 5 and 7 (MJD 59704 and 59706), within the Polarimetric Monitoring of AGN at Millimeter Wavelengths (POLAMI) program (Agudo et al. 2018b,a). Under the POLAMI[4] observing setup, the four Stokes parameters (I, Q, U, and V) are recorded simultaneously using the XPOL procedure (Thum et al. 2008). We reduced, calibrated, and managed the data following the POLAMI procedure described in detail in Agudo et al. (2018b). In the two measurements at 3.5 mm, the source flux density increased from 0.278 ± 0.014 Jy to 0.384 ± 0.019 Jy, while at the same time the polarization properties remained relatively stable (see Table 1). Only one measurement was taken at 1.3 mm, on 2022 May 7, providing an upper limit at 95% confidence level of 6% for the degree of polarization.

REFERENCES

[3] https://people.bu.edu/clemens/mimir/index.html
[4] http://polami.iaa.es/

Abdo, A. A., Ackermann, M., Ajello, M., et al. 2011, ApJ, 736, 131, doi: 10.1088/0004-637X/736/2/131

Agudo, I., Thum, C., Ramakrishnan, V., et al. 2018a, MNRAS, 473, 1850, doi: 10.1093/mnras/stx2437

Agudo, I., Thum, C., Molina, S. N., et al. 2018b, MNRAS, 474, 1427, doi: 10.1093/mnras/stx2435

Angelakis, E., Hovatta, T., Blinov, D., et al. 2016, MNRAS, 463, 3365, doi: 10.1093/mnras/stw2217

Arnaud, K., Dorman, B., & Gordon, C. 1999, XSPEC: An X-ray spectral fitting package. http://ascl.net/9910.005

Baldini, L., Bucciantini, N., Di Lalla, N., et al. 2022, arXiv e-prints, arXiv:2203.06384. https://arxiv.org/abs/2203.06384

Baloković, M., Paneque, D., Madejski, G., et al. 2016, ApJ, 819, 156, doi: 10.3847/0004-637X/819/2/156

Blandford, R., & Eichler, D. 1987, PhR, 154, 1, doi: 10.1016/0370-1573(87)90134-7

Blandford, R., Meier, D., & Readhead, A. 2019, ARA&A, 57, 467, doi: 10.1146/annurev-astro-081817-051948

Blinov, D., Pavlidou, V., Papadakis, I., et al. 2015, MNRAS, 453, 1669, doi: 10.1093/mnras/stv1723

Bodo, G., Tavecchio, F., & Sironi, L. 2021, MNRAS, 501, 2836, doi: 10.1093/mnras/staa3620

Böttcher, M., Reimer, A., Sweeney, K., & Prakash, A. 2013, ApJ, 768, 54, doi: 10.1088/0004-637X/768/1/54

Clemens, D. P., Pinnick, A. F., & Pavel, M. D. 2012, ApJS, 200, 20, doi: 10.1088/0067-0049/200/2/20

Costa, E., Soffitta, P., Bellazzini, R., et al. 2001, Nature, 411, 662. https://arxiv.org/abs/astro-ph/0107486

Di Gesu, L., Tavecchio, F., Donnarumma, I., et al. 2022, arXiv e-prints, arXiv:2201.09597. https://arxiv.org/abs/2201.09597

Donnarumma, I., Vittorini, V., Vercellone, S., et al. 2009, ApJL, 691, L13, doi: 10.1088/0004-637X/691/1/L13

Ferrazzoli, R., Muleri, F., Lefevre, C., et al. 2020, Journal of Astronomical Telescopes, Instruments, and Systems, 6, 048002, doi: 10.1117/1.JATIS.6.4.048002

Ghisellini, G., & Tavecchio, F. 2009, MNRAS, 397, 985, doi: 10.1111/j.1365-2966.2009.15007.x

HI4PI Collaboration, Ben Bekhti, N., Flöer, L., et al. 2016, A&A, 594, A116, doi: 10.1051/0004-6361/201629178

Hovatta, T., Lindfors, E., Blinov, D., et al. 2016, A&A, 596, A78, doi: 10.1051/0004-6361/201628974

Hughes, P. A., Aller, H. D., & Aller, M. F. 1985, ApJ, 298, 301, doi: 10.1086/163611

Hughes, P. A., & Miller, L. 1991, in Beams and Jets in Astrophysics, Vol. 19, 1

Kirk, J. G., Rieger, F. M., & Mastichiadis, A. 1998, A&A, 333, 452. https://arxiv.org/abs/astro-ph/9801265

Kislat, F., Clark, B., Beilicke, M., & Krawczynski, H. 2015, Astroparticle Physics, 68, 45, doi: 10.1016/j.astropartphys.2015.02.007

Komissarov, S. S., Barkov, M. V., Vlahakis, N., & Königl, A. 2007, MNRAS, 380, 51, doi: 10.1111/j.1365-2966.2007.12050.x

Lin, Y. C., Bertsch, D. L., Chiang, J., et al. 1992, ApJL, 401, L61, doi: 10.1086/186671

Liodakis, I., Peirson, A. L., & Romani, R. W. 2019, ApJ, 880, 29, doi: 10.3847/1538-4357/ab2719

MAGIC Collaboration, Acciari, V. A., Ansoldi, S., et al. 2021, A&A, 655, A89, doi: 10.1051/0004-6361/202141004

Marscher, A. P. 2008, in Astronomical Society of the Pacific Conference Series, Vol. 386, Extragalactic Jets: Theory and Observation from Radio to Gamma Ray, ed. T. A. Rector & D. S. De Young, 437

Marscher, A. P. 2014, ApJ, 780, 87, doi: 10.1088/0004-637X/780/1/87

Marscher, A. P., & Gear, W. K. 1985, ApJ, 298, 114, doi: 10.1086/163592

Marscher, A. P., & Jorstad, S. G. 2021, Galaxies, 9, 27, doi: 10.3390/galaxies9020027

Marshall, H. L. 2021, AJ, 162, 134, doi: 10.3847/1538-3881/ac173d

Massaro, E., Perri, M., Giommi, P., & Nesci, R. 2004, A&A, 413, 489, doi: 10.1051/0004-6361:20031558

Matthews, J. H., Bell, A. R., & Blundell, K. M. 2020, NewAR, 89, 101543, doi: 10.1016/j.newar.2020.101543

Nilsson, K., Pasanen, M., Takalo, L. O., et al. 2007, A&A, 475, 199, doi: 10.1051/0004-6361:20077624

Nilsson, K., Lindfors, E., Takalo, L. O., et al. 2018, A&A, 620, A185, doi: 10.1051/0004-6361/201833621

Pesce-Rollins, M., Lalla, N. D., Omodei, N., & Baldini, L. 2019, Nuclear Instruments and Methods in Physics Research A, 936, 224, doi: 10.1016/j.nima.2018.10.041

Piner, B. G., & Edwards, P. G. 2005, ApJ, 622, 168, doi: 10.1086/428039

Punch, M., Akerlof, C. W., Cawley, M. F., et al. 1992, Nature, 358, 477, doi: 10.1038/358477a0

Rankin, J., Muleri, F., Tennant, A. F., et al. 2022, AJ, 163, 39, doi: 10.3847/1538-3881/ac397f

Romero, G. E., Boettcher, M., Markoff, S., & Tavecchio, F. 2017, SSRv, 207, 5, doi: 10.1007/s11214-016-0328-2

Sironi, L., Petropoulou, M., & Giannios, D. 2015, MNRAS, 450, 183, doi: 10.1093/mnras/stv641

Sironi, L., & Spitkovsky, A. 2014, ApJL, 783, L21, doi: 10.1088/2041-8205/783/1/L21

Soffitta, P., Baldini, L., Bellazzini, R., et al. 2021, AJ, 162, 208, doi: 10.3847/1538-3881/ac19b0

Strohmayer, T. E. 2017, ApJ, 838, 72, doi: 10.3847/1538-4357/aa643d

Tavecchio, F. 2021, Galaxies, 9, 37, doi: 10.3390/galaxies9020037

Tavecchio, F., Landoni, M., Sironi, L., & Coppi, P. 2018, MNRAS, 480, 2872, doi: 10.1093/mnras/sty1491

Tchekhovskoy, A., Narayan, R., & McKinney, J. C. 2011, MNRAS, 418, L79, doi: 10.1111/j.1745-3933.2011.01147.x

Thum, C., Wiesemeyer, H., Paubert, G., Navarro, S., & Morris, D. 2008, PASP, 120, 777, doi: 10.1086/590190

Weaver, Z. R., Jorstad, S. G., Marscher, A. P., et al. 2022, ApJS, 260, 12, doi: 10.3847/1538-4365/ac589c

Weisskopf, M. 2022, in AAS/High Energy Astrophysics Division, Vol. 54, AAS/High Energy Astrophysics Division, 301.01

Wilms, J., Allen, A., & McCray, R. 2000, ApJ, 542, 914, doi: 10.1086/317016

Zhang, H., Li, X., Giannios, D., & Guo, F. 2021, ApJ, 912, 129, doi: 10.3847/1538-4357/abf2be

Zhang, H., Li, X., Guo, F., & Giannios, D. 2018, ApJL, 862, L25, doi: 10.3847/2041-8213/aad54f